

A New Statistical Estimate of the Radar Coverage of the Low Earth Orbit Debris Environment

Chris L. Ostrom

HX5 Jacobs JETS Contract, NASA Johnson Space Center
christopher.l.ostrom@nasa.gov

Timothy F. Kennedy

NASA Johnson Space Center, Orbital Debris Program Office

ABSTRACT

For over three decades, the NASA Orbital Debris Program Office (ODPO) has used the Goldstone Orbital Debris Radar, Haystack Ultrawideband Satellite Imaging Radar (HUSIR), and Haystack Auxiliary (HAX) radar assets to collect data on the low Earth orbit (LEO) debris environment. Each radar, with its unique beamwidth, altitude and inclination coverage, and limiting size threshold, operates in a beam park mode to statistically sample the orbital debris population in LEO. Provided that these assets are shared with other users, the orbital debris data collection is not continuous; rather, intermittent data collects are acquired and sent to the NASA ODPO. To understand the sampling process conducted by each radar over time and any related observational biases, a Statistical Confirmation of Radar Uniformity or Bias (SCRUB) code has been implemented to model the coverage of these assets for informing future operations, as well as usage of the data collected from these ground-based sensors. For this analysis, Right Ascension of the Ascending Node (RAAN) is used as a metric to measure statistical coverage. A complete survey of the LEO environment is understood to be measurements that sufficiently sample all values of RAAN for each altitude-inclination pair visible from the radar asset. Regions of incompleteness or statistical bias can help inform future observation campaigns.

The SCRUB tool evaluates the coverage of the LEO environment, not by examining individual objects that may pass through a sensor's field of view (FOV), but by determining which orbit planes pass through the FOV. Once a pointing geometry for a radar site, observation time, and range extent are configured by the user, SCRUB computes the inclinations and altitudes that are visible by the sensor. For each inclination-altitude pair, there is a distinct pair of possible RAAN values, corresponding to the ascending and descending orbit passing through that point in the sensor cone. Repeating this process for all points in the beam, and for multiple time periods during an observation window, creates a matrix of all inclination-altitude-RAAN combinations that are visible during a sensor run. This process can then be repeated for all observations within a year (for an annual survey), propagating all the RAAN values to a common epoch, typically the start of a calendar year, and combining the observations to assemble a full estimate of the RAAN coverage of the LEO environment. This RAAN coverage can then be analyzed for uniformity of sampling, within a certain inclination-altitude pair, or between larger regions of the space environment.

This paper provides a general overview of the radar assets utilized by ODPO, typical analysis data products assuming circular orbits, and a discussion of the algorithms that feed between modeling and measurement operations. Following the description of the algorithm, estimates of coverage using HUSIR radar data collected from multiple years are developed and compared.

1. INTRODUCTION

Since 1990, the NASA Orbital Debris Program Office (ODPO) has relied on ground-based radar measurements to characterize the distribution of orbital debris (OD) in low Earth orbit (LEO) that is too small to be tracked by the U.S. Space Surveillance Network (SSN), down to a limiting size determined by the sensitivity of each radar [1, 2]. The ODPO does not use radar measurements to track orbital debris. Instead, the radars are operated in a beam park mode, whereby the radar is pointed to a particular elevation and azimuth angle, which may be referred to as a pointing geometry, and OD is detected as it travels through the radar beam. Measurements from the radar typically include the range and range-rate information of the detected object, as well as estimates of the radar cross sections

measured in two orthogonal circular polarizations. The ground-based radars are operated in beam park mode, with the intent to statistically sample the orbital debris environment in LEO. The statistical samples of the OD environment are then used in the process of building OD models, scaling the OD populations in the models to match the measurements. Additionally, radar measurements that are not used in the OD model building process are used for model validation purposes.

Since OD radar measurements are intended to sample the OD environment, understanding the sampling distribution is of interest to determine whether there are biases, as well as under- or over-sampling of particular orbits that needs to be accounted for in using the radar measurement data. Determining and monitoring the sampling distribution throughout the data collection process also is of interest to help guide the operations teams at the different radar sites on the best times to conduct measurements.

2. BEAM PARK MODE DATA COLLECTION

Typically, several assumptions are made for the radar data collected by sampling the OD environment using beam park mode. These assumptions include an approximately uniform distribution of OD in Right Ascension of the Ascending Node (RAAN); data collection using the radar sufficiently samples all possible RAANs; OD in LEO are in circular orbits; and depending upon the model being employed, only one OD object travels through the radar beam at a time. Several of these assumptions have been considered elsewhere [3, 4] and are not discussed in detail in this paper. The focus of this work is to understand the sampling biases that may be present in a given collection of radar data such that these can better inform the use of the data for modeling and understanding of the OD environment.

Fig. 1 shows a depiction of the Haystack Ultrawideband Satellite Imaging Radar (HUSIR) radar operating in a beam park mode, where the narrow pencil beam of the radar is pointed at an elevation and azimuth angle and allowed to sample the OD environment. As the Earth rotates, the radar beam samples from a fixed volume of space. The beam widths of the ground-based radars used for OD observations are typically very narrow. HUSIR has a 3 dB beam width of 0.058° , and the region of space sampled is approximately a surface of revolution, shown in red in Fig. 1 for the HUSIR 75° elevation and due East (75E) pointing geometry. Based on the sampling region shown, the orbits that may be detected by the radar are dependent upon the latitude of the sensor, the range window of the radar, and the pointing geometry used. Additionally, the lower bound on OD sizes that may be detected is dependent on the sensitivity of the radar and the slant range to the object detected. With the 75E-pointing geometry and latitude of the sensor, HUSIR is limited to orbit inclinations of approximately 42° [5].

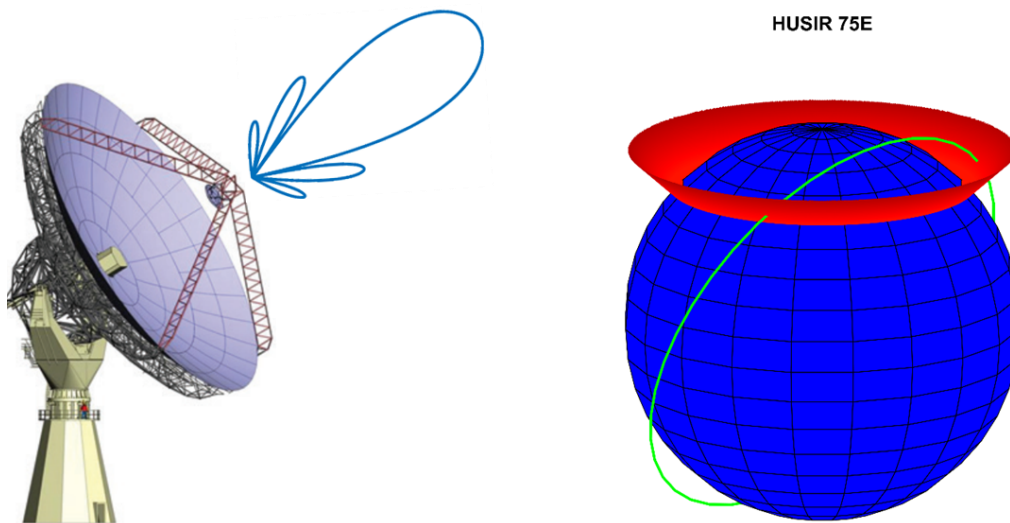


Fig. 1. HUSIR operating in a beam park mode (left), and sampled region of space for the 75E pointing geometry (right). HUSIR CAD Model reprinted with permission courtesy of MIT Lincoln Laboratory, Lexington, Massachusetts.

Orbit inclination is not a parameter that may be inferred precisely from the radar measurements while operating in a beam park mode due to the short arc observation of an OD object passing through the narrow radar beam. Approximating a detected OD object's orbit as circular; however, it is often possible to infer a circular orbit for the object from the range and range-rate information. Inclination calculated in this fashion is referred to as the Doppler inclination for the object. Based on Doppler inclination and altitude measurements, it is possible to observe the different orbit families in LEO. Fig. 2 shows OD objects detected by HUSIR 75E from U.S. Government fiscal year (FY) 2014 through 2017 [6]. Also highlighted are several on-orbit fragmentation events, denoted with red circles. The center of each circle is located at the altitude and inclination at the time of the event; more details surrounding these breakups can be found in the History of On-Orbit Satellite Fragmentations [7]. The dashed black curve shows the sun-synchronous constraint for circular orbits having a given inclination. Note the distinct clusters of OD objects that show up in the radar measurement data near the highlighted events, or for OD originating from sun-synchronous orbits.

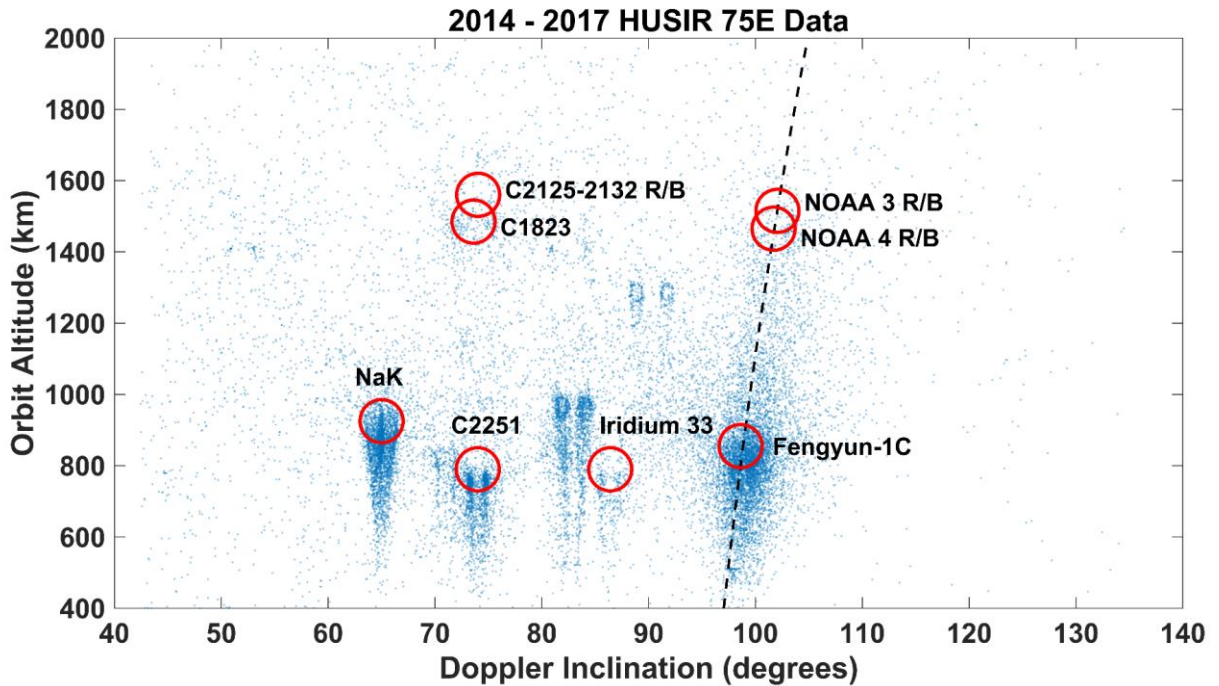


Fig. 2. Orbit altitude vs Doppler Inclination observations made in FY2014 - 2017 by HUSIR. Doppler inclination is a derived parameter under the assumption of a circular orbit.

3. SCRUB TOOL METHODOLOGY

Radar measurements of detected objects are typically given in a range-azimuth-elevation frame, from a point on the surface of the Earth ellipsoid – namely the radar site. For the formulation that follows, the location of the radar site, \vec{R} , in an Earth-Centered, Earth-Fixed (ECEF) coordinate frame is described in Eq. 1. The vector, $\vec{\rho}$, from the radar site to the OD object detected in the East-North-Up (ENU) coordinate frame is shown in Eq. 2, where the range, ρ , elevation angle, El , and azimuth angle, Az , are depicted in Fig. 3. To convert the position of the detected OD from ENU to ECEF coordinates, the matrix, Q_{xx} , is applied as shown in Eq. 3 and 4, where λ and ϕ_{gd} are the longitude and geodetic latitude of the radar site, respectively. The resulting vector, \vec{r} , is the location of the OD detected by the radar in ECEF coordinates. The geocentric latitude, ϕ_c , and the longitude, λ_{beam} , for the OD object in the beam of the radar are then determined, as described in Eq. 5 and 6. Both ϕ_c and λ_{beam} are illustrated for the detected OD object in Fig. 3.

$$\vec{R} = \begin{bmatrix} x_0 \\ y_0 \\ z_0 \end{bmatrix} \quad (1)$$

$$\vec{\rho} = \begin{bmatrix} -\rho \cos(El) \cos(Az) \\ \rho \cos(El) \sin(Az) \\ \rho \sin(El) \end{bmatrix} \quad (2)$$

$$Q_{xx} = \begin{bmatrix} -\sin(\lambda) & \sin(\phi_{gd}) \cos(\lambda) & \cos(\phi_{gd}) \cos(\lambda) \\ \cos(\lambda) & \sin(\phi_{gd}) \sin(\lambda) & \cos(\phi_{gd}) \sin(\lambda) \\ 0 & \cos(\phi_{gd}) & \sin(\phi_{gd}) \end{bmatrix} \quad (3)$$

$$\vec{r} = \vec{R} + Q_{xx} \vec{\rho} \quad (4)$$

$$\phi_c = \arcsin\left(\frac{r_z}{r}\right) \quad (5)$$

$$\lambda_{beam} = \arctan\left(\frac{r_y}{r_x}\right) \quad (6)$$

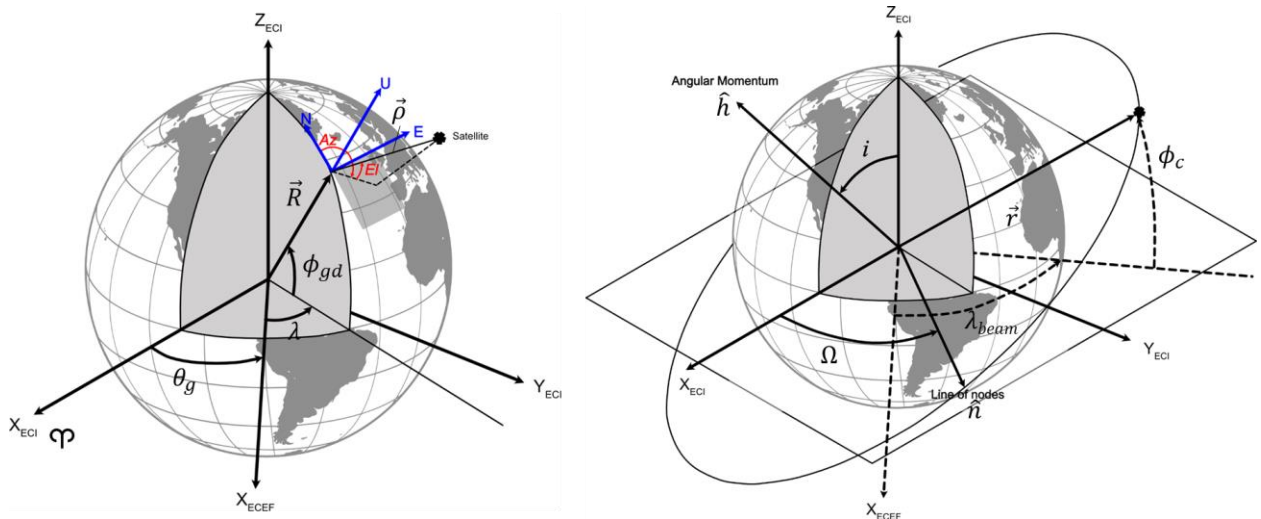


Fig. 3. Location of the radar site in ECI and ECEF coordinates and detected OD object location in ENU coordinates (left). Orbital elements for the satellite detected by the radar (right).

Once the geocentric latitude and longitude are determined for the OD object, circular orbital elements may be determined. Of interest are the object's inclination, i , and RAAN, Ω , assuming the object is in a circular orbit. The feasible set of inclinations that may be observed are limited to those values between approximately ϕ_c and $180 - \phi_c$, inclusive, as objects having inclinations outside of that range will not be visible from the radar site. Note that for lower elevation angle pointing geometries, the set of observable inclinations does increase; however, the majority of observations are conducted using a 75E pointing geometry for HUSIR – which are approximately limited to the inclinations described previously. Similarly, 75E pointing geometries are typically used for HAX and Goldstone as well. As such, possible inclinations that may be observed are limited to approximately $[\phi_c, 180 - \phi_c]$ for the purposes of discussion in this paper.

To apply the Statistical Confirmation of Radar Uniformity or Bias (SCRUB) tool, the interval of possible inclinations is sampled, and for each inclination, two RAANs are calculated – corresponding to orbital debris that is detected while on the ascending or descending part of its orbit. The difference in longitude from the ascending node

to λ_{beam} is ΔLAN , as depicted in Fig. 4, and is determined using Eq. 7. A correction to account for the rotation of the Earth that occurs from the time of ascending nodal crossing to when the radar site observes the satellite is made by first computing the argument of latitude, u_1 , as shown in Eq. 8. The longitude correction, $\Delta\lambda_{rot}$, is then calculated using Eq. 9, where n is the mean motion. Using these results, the first possible RAAN for a sampled inclination, Ω_1 , is determined using Eq. 10, where θ_g is the Greenwich Mean Sidereal Time (GMST) in degrees at the time of detection. The GMST, θ_g , at the time of detection is depicted in Fig. 3 and is the angle between the X-axis (the vernal equinox direction, $\overline{\mathcal{P}}$) in the Earth-centered inertial (ECI) frame, and the X-axis in the ECEF frame.

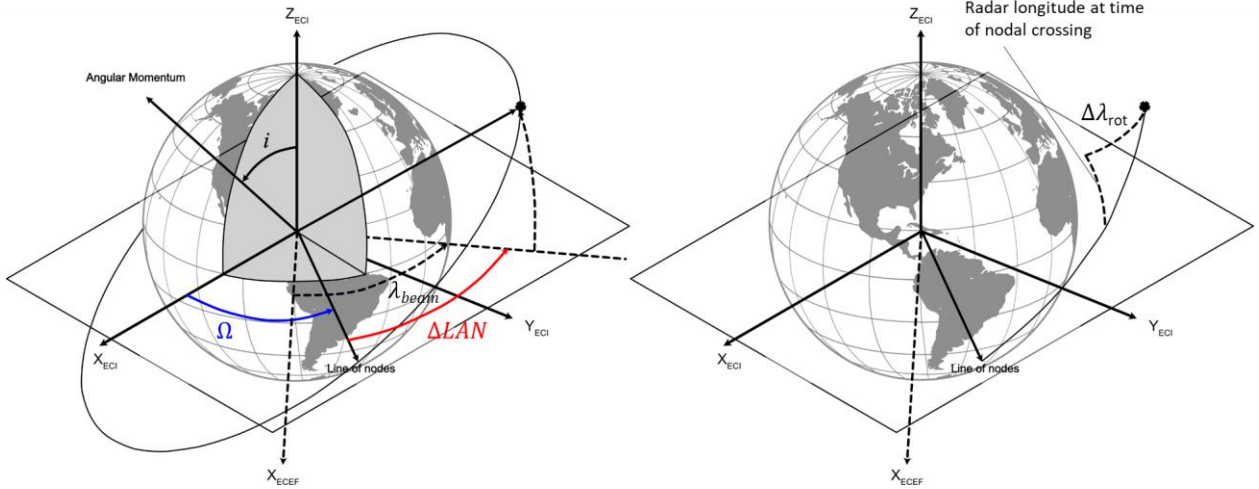


Fig. 4. Terms involved in the calculation of RAAN at the time of measurement by the radar (left). There is an additional change in longitude needed, $\Delta\lambda_{rot}$, to account for the Earth rotation between time at the node crossing and the observation by the radar (right).

$$\Delta LAN = \arcsin\left(\frac{\tan(\phi_c)}{\tan(i)}\right) \quad (7)$$

$$u_1 = \arcsin\left(\frac{\sin(\phi_c)}{\sin(i)}\right) \quad (8)$$

$$\Delta\lambda_{rot_1} = \frac{u_1}{n} \quad (9)$$

$$\Omega_1 = \lambda_{beam} - \Delta LAN + \Delta\lambda_{rot_1} + \theta_g \text{ mod } 360 \quad (10)$$

GMST is calculated using Eqs. 11 – 15, where JD is the Julian date, T_0 is number of Julian centuries elapsed from the J2000.0 epoch, $\theta_{g,0}$ is the GMST at midnight in degrees, and UT is the elapsed time since midnight in hours [8].

$$JD = 367 * \text{year} - \left\lfloor \frac{7}{4} * \text{year} + \left\lfloor \frac{\text{month} + 9}{12} \right\rfloor \right\rfloor + \left\lfloor \frac{275 * \text{month}}{9} \right\rfloor + \text{day} + 1721013.5 \quad (11)$$

$$T_0 = \frac{JD - 2451545}{36525} \quad (12)$$

$$\theta_{g,0} = 100.4606184 + 36000.77005361T_0 + 3.8793 * 10^{-4}T_0^2 - 2.583 * 10^{-8}T_0^3 \text{ mod } 360 \quad (13)$$

$$UT = hour + \frac{minute}{60} + \frac{second}{3600} \quad (14)$$

$$\theta_g = \theta_{g,0} + 360.98564724 \frac{UT}{24} \quad (15)$$

The second possible RAAN, Ω_2 , for a sampled inclination is calculated using Eq. 16. The calculations are like that shown in Eq. 7 – 10; however, the argument of latitude is modified as shown in Eq. 17, which produces a different time since the node crossing for the descending part of the orbit. For a better comparison of the results using SCRUB, all RAAN values are propagated to a common epoch using Eqs. 19 and 20 – since an aspherical Earth and the asymmetrical gravity model cause nodal precession for measurements made over time. The nodal precession rate is $\dot{\Omega}$, and the Δt is the time difference from the observation time to the common epoch (positive or negative). The nodal precession rate, in degrees per day, is computed using Eq. 21, where J_2 is the second zonal Earth gravity harmonic, SMA is the semi-major axis of the orbit (the magnitude of \vec{r} since circular orbits are assumed), n is the mean motion, i is the orbit inclination, and r_E is the average radius of the Earth.

$$\Omega_2 = \lambda_{beam} - \Delta LAN + \Delta \lambda_{rot_2} + \theta_g \text{ mod } 360 \quad (16)$$

$$u_2 = 180^\circ - u_1 \quad (17)$$

$$\Delta \lambda_{rot_2} = \frac{u_2}{n} \quad (18)$$

$$\Omega_1^0 = \Omega_1 + \dot{\Omega} \Delta t \text{ mod } 360 \quad (19)$$

$$\Omega_2^0 = \Omega_2 + \dot{\Omega} \Delta t \text{ mod } 360 \quad (20)$$

$$\dot{\Omega} = -540 * J_2 * \left(\frac{r_E}{SMA} \right)^2 * n * \cos(i) \quad (21)$$

The full SCRUB algorithm is outlined in the following steps:

1. Select the sample sizes for range, inclination, and RAAN.
2. Select a point in time.
3. Select a point of interest along the radar beam, using the azimuth and elevation pointing angles, and a sampled range.
4. Determine the interval of feasible inclinations.
5. For each inclination at the selected step size:
 - a. Compute the two possible RAAN values
 - b. Correct for nodal precession, propagating to a common epoch – typically the first day of the year of interest
 - c. Add a count to a data structure that tracks the number of times a given (altitude, inclination, RAAN) tuple may be observed by the radar. Counts are added to the appropriate altitude, inclination, and RAAN bin.
6. Repeat steps 3 – 5 for the set of range or altitude samples that are observable for the radar.

4. EXAMPLE CALCULATIONS USING SCRUB

During a HUSIR observation window that started on 6 January 2015 15:21Z, a slant range of 200 km is selected as the initial range sample for examination. The radar is pointed 75E, and with the selected range and using Eq. 2, the location in ENU coordinates is shown Eq. 21. Transformation of this point to ECEF coordinates using Eq. 3 produces the result shown in Eq. 22. The longitude and geocentric latitude at \vec{r} are then calculated, with the results shown in Eqs. 23 and 24. As discussed previously, inclination limits are established by the geocentric latitude, which for this example restricts the inclination between 42.435° and 137.565°. For this example, an inclination equal to 42.435° is chosen for further examination. Note that in applying the SCRUB methodology, all inclinations within the inclination limits, at the specified inclination step size, will have the same process applied. Also, while the final counts for each altitude, inclination, and RAAN tuple are binned, intermediate calculations are carried out using more precision. Typical step sizes used are approximately 0.1° for inclination, 1° for RAAN, and 21 km for range.

$$\vec{\rho} = \begin{bmatrix} -200\cos(75^\circ)\cos(90^\circ) \\ 200\cos(75^\circ)\sin(90^\circ) \\ 200\sin(75^\circ) \end{bmatrix} = \begin{bmatrix} 51.763 \\ 0 \\ 193.185 \end{bmatrix} \text{ km} \quad (21)$$

$$\vec{r} = \begin{bmatrix} 1492.405 \\ -4457.405 \\ 4296.880 \end{bmatrix} + Q_{xx} \begin{bmatrix} 51.763 \\ 0 \\ 193.185 \end{bmatrix} = \begin{bmatrix} 1586.622 \\ -4575.765 \\ 4427.700 \end{bmatrix} \text{ km} \quad (22)$$

$$\phi_c = \arcsin\left(\frac{4427.700}{6561.975}\right) = 42.435^\circ \quad (23)$$

$$\lambda_{beam} = \arctan\left(\frac{-4575.765}{1586.622}\right) = -70.876^\circ E \quad (24)$$

At the observation time, the corresponding GMST is determined using Eqs. 11 – 15, and the two possible RAANs are then determined using Eq. 10 and 16. The results of these calculations are that θ_g is 264.277°, Ω_1 is 354.277°, and Ω_2 is 174.277°. The remaining step for this pair of RAANs is to compute the precession of the nodes between the observation time and the common epoch of 1 January 2015 00:00Z. The results using Eqs. 18 and 19 are that Ω_1^0 is 316.730° and Ω_2^0 is 136.730°. We assume that the length of an observation window is small relative to the time from the common epoch. This may be corrected by breaking the observation window into multiple time steps, and then sampling from these smaller time steps instead of just at the beginning or end of an observation window. The data structure that tracks the number of times a given altitude, inclination, and RAAN tuple is observed by the radar is then incremented by one. A slice of the data in RAAN after the first update is depicted in Fig. 5, which shows that two RAANs identified using SCRUB have been observed. Note that the bin size in RAAN shown in Fig. 5 is larger than the typical 1° step size for clarity.

The end of the HUSIR observation window on 6 January 2015 is at 15:55Z. Conducting a similar process to that at the beginning of the observation window, the GMST, corresponding RAANs, and precession-corrected RAANs to the common epoch are calculated. The results are that θ_g is 272.800°, Ω_1 is 2.800°, Ω_2 is 182.800°, Ω_1^0 is 325.253° and Ω_2^0 is 145.253°. Hence, the bounds on RAAN for this particular range and inclination sample during the observation window are summarized in Eq. 25 using a 1° bin size for RAAN. All RAANs identified in this range have their count incremented within the data structure tracking each altitude, inclination, and RAAN tuple. As described in Section 3, the process is then repeated for each possible altitude and inclination sample pair that may be observed for the radar pointing within the observation window.

$$\Omega \in [137^\circ, 145^\circ] \cup [317^\circ, 325^\circ] \quad (25)$$

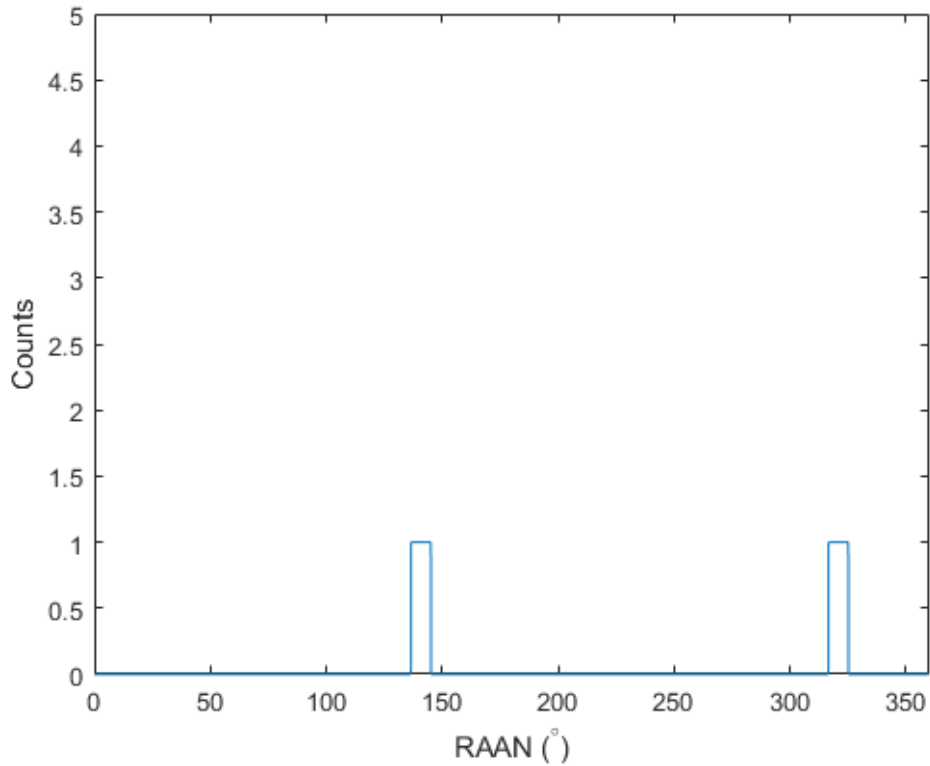


Fig. 5. RAAN counter for 200 km range and 42.4° (42.435°) inclination after one set of observations.

5. INITIAL SCRUB RESULTS

SCRUB was applied to multiple years of HUSIR observations to assess the characteristics of the sampling distribution in altitude, inclination, and RAAN. To summarize the frequency of RAAN observations in a given year, the minimum, maximum, as well as a measure of the spread of the RAAN counts in a given year are considered in this section. Shown in Fig. 6 are the minimum and maximum RAAN counts for each altitude and inclination pair for HUSIR measurement window times in FY2016. Data was binned to approximately 0.1° in inclination, 1° in RAAN, and 21 km in range to generate the results shown. Each altitude and inclination pair has a range of RAAN values on the interval $[0^\circ, 360^\circ)$, excluding identically the value 360°. The RAAN with the minimum number of counts observed within each altitude and inclination pair, as well as the RAAN with the maximum number of counts observed were recorded and used to generate the plots for Fig. 6. As shown in Fig. 6, all RAANs are observed at least once for each altitude and inclination pair, and in many cases the minimum number of observations is at least 20. Also shown in Fig. 6, the maximum number of times a given RAAN was observed is typically in the range of 40–60 counts.

A measure of the spread between the minimum and maximum number of RAAN counts for each altitude and inclination pair is shown in Fig. 7. The typical spread between the maximum and minimum RAAN counts, as shown in Fig. 7, is in the range of 20–40 counts. There appears to be some altitude and inclination pairs that have a wider spread in RAAN counts than others. These regions have a greater maximum number of counts in Fig. 6, which also coincides in some instances with RAANs having fewer minimum number of counts. Note that the largest clusters of altitude and inclinations receiving the highest number of maximum RAAN counts are for inclinations near the latitude of the sensor. Also of interest is that the symmetry observed in Figs. 6 and 7 indicates that the radar has a similar sampling distribution for prograde and retrograde orbits.

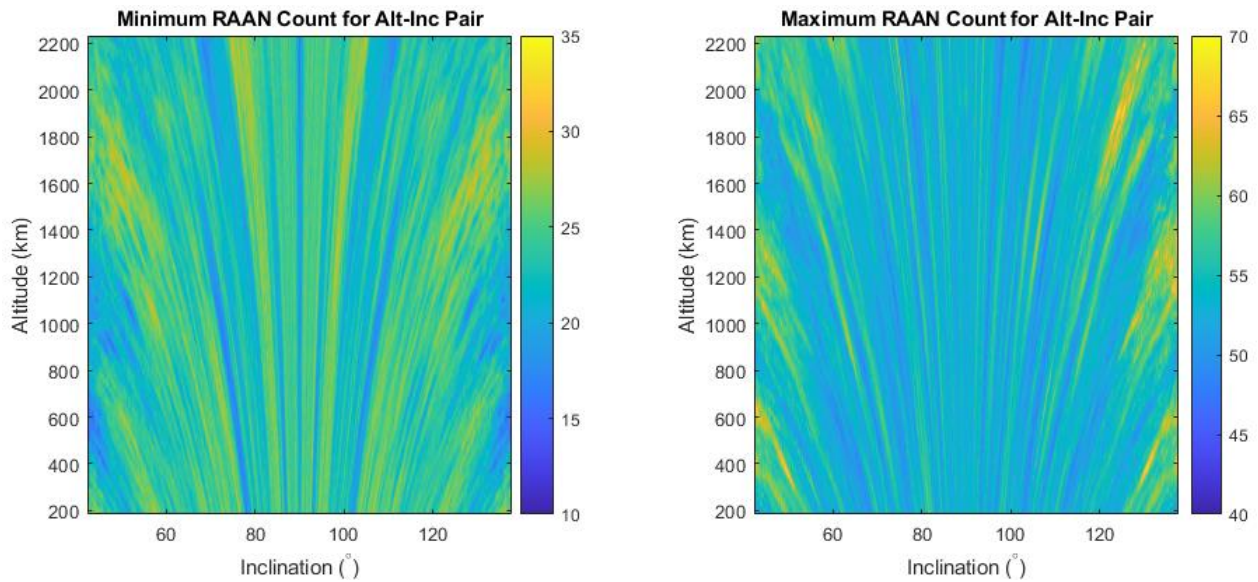


Fig. 6. FY16 Minimum and maximum RAAN counts for each altitude and inclination pair.

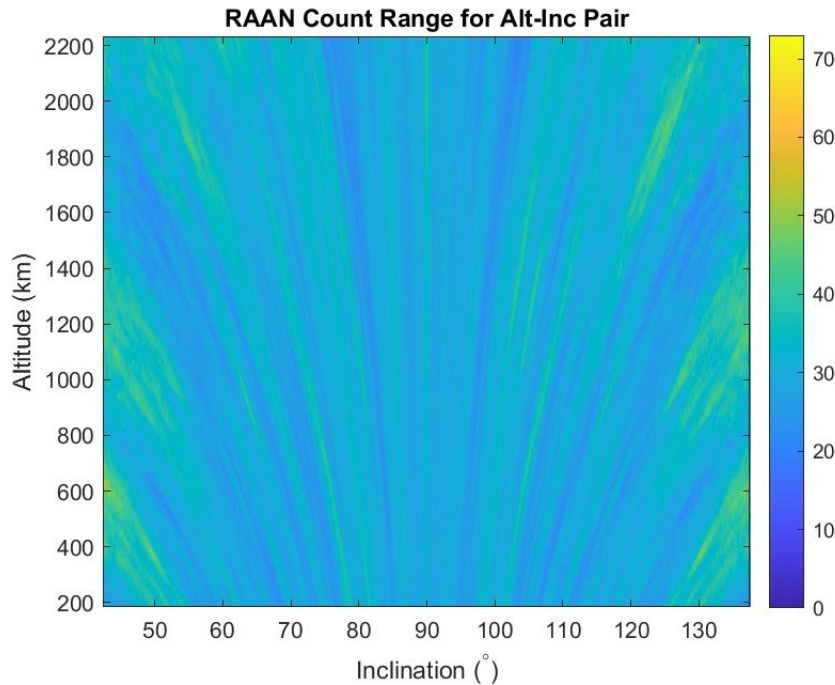


Fig. 7. FY16 Range of RAAN counts, difference between maximum and minimum, for each altitude and inclination pair.

Similar to the results from HUSIR in FY16, the minimum and maximum RAAN counts for each altitude and inclination pair for HUSIR FY17 measurement times are shown in Fig. 8. The spread between the minimum and maximum RAAN counts for each altitude and inclination pair are shown in Fig. 9. Clustering in the maximum RAAN counts for certain altitude and inclinations is again evident. The largest clustering (again) appears near the latitude of the sensor for certain altitude and inclination pairs. These pairs also showed the most variation between RAANs sampled in these regions. Polar and near polar orbits have similar clustering of the maximum RAAN count sampling characteristics in FY17 – with the effect appearing to be independent of altitude for these orbits. Although these regions do see more variation in RAAN sampling, the minimum times a RAAN was sampled for a given

altitude and inclination pair is typically at least 20, and there are no instances where a RAAN was missed for a given altitude and inclination pair.

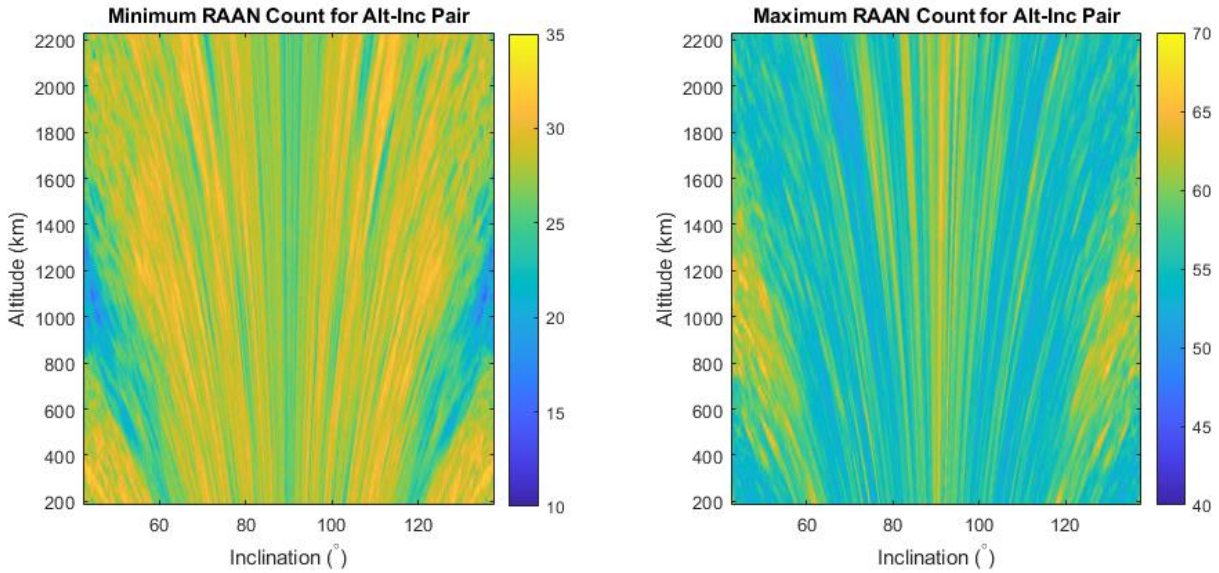


Fig. 8. FY17 Minimum and maximum RAAN counts for each altitude and inclination pair.

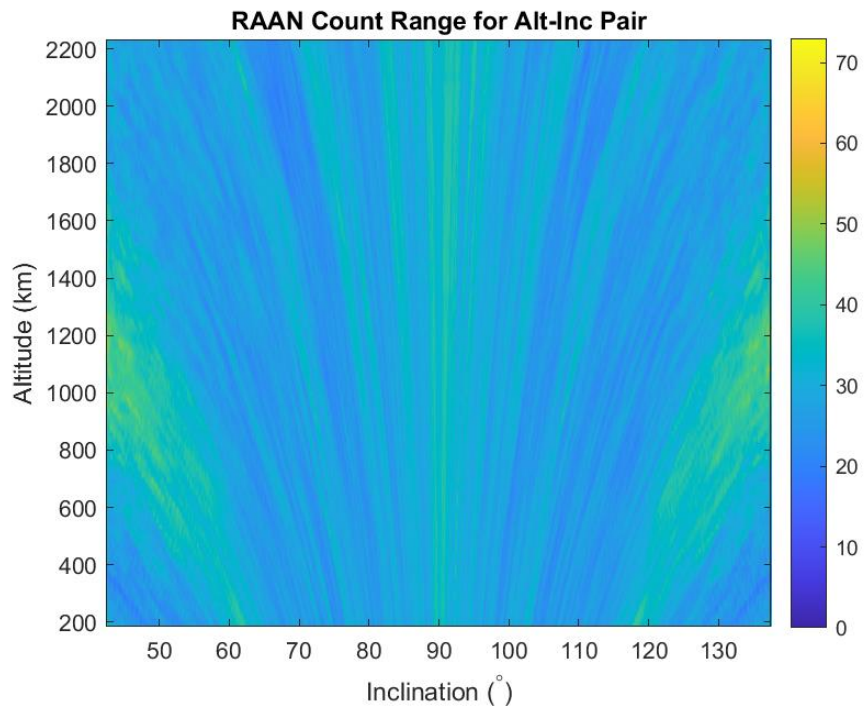


Fig. 9. FY17 Range of RAAN counts, difference between maximum and minimum, for each altitude and inclination pair.

6. CONCLUSIONS AND FUTURE WORK

The SCRUB tool, discussed in this paper, outlines a method that enables estimating the sampling distribution for the radar during a particular time period. Initial results from applying SCRUB to radar measurement time windows indicate that some orbits are sampled more frequently than others by the radar, and that some pairs of altitude and inclination see more variation in the RAAN sampling than others. It is interesting to note that some sun-

synchronous orbits may be included in the orbits that see more variation in the RAAN sampling; however, the data collection process does not appear to have any bias towards these orbits relative to other altitude and inclination pairs. Clustering of radar measurements within the sun-synchronous regime has been a long-standing question of interest [4]. Many altitude and inclination regions are well-sampled without specifically planning for equitemporal observations, and there were no instances where a RAAN was missed for a given altitude and inclination. For altitude and inclination regions where orbits are sampled more frequently, time-weighting may be a factor in these counts, and additional analysis is needed. While variation in the RAAN distribution is not ideal, having an improved understanding of the sampling distribution allows for applying statistical corrections to the observations or to specific populations, as well as providing a method to plan radar measurement times to improve the sampling performance of the OD environment. SCRUB is expected to become a useful tool for informing OD models that make use of the radar measurement data. This may include updated models with different RAAN populations, much like Molniya-type orbits that have different argument of perigee (AOP) populations.

Note that the results presented are still being validated, and that as the tool is developed for understanding yearly radar observations, updates and improvements are expected. The basic SCRUB algorithm that was discussed in this paper included several simplifying assumptions that may be explored in future work. The radar sensors that collect orbital debris data for the NASA ODPO have a very narrow beamwidth, $< 0.1^\circ$, making the treatment of the radar beam as having zero beamwidth a reasonable choice. For radars having wider beamwidths, SCRUB will need to be modified to include the effects of the beamwidth in the algorithm. Also, the examples and use cases investigated to date are limited to LEO orbital periods and circular orbits. Including the effects of eccentricity and longer period orbits may require updates to the algorithm. For the case of eccentric orbits, the parameter space increases from considering two RAANs for each altitude and inclination pair, to two AOPs and two RAANs for each eccentricity considered. Additionally, one envisioned use of SCRUB is for observation planning, i.e., determining observation times of interest to either improve sampling of under-sampled orbits or to avoid over-sampling to the extent possible. This will require additional algorithm development and testing, since using SCRUB as an observational planning tool is essentially the inverse operation of the algorithm described in this paper. A possible workflow for the planning tool would be to run SCRUB to determine the current sampling distribution and identify areas of over- or under-sampling, and then conduct the inverse operation to identify candidate observation times.

7. REFERENCES

- [1] Murray, J., Kennedy, T., “Haystack Ultra-wideband Satellite Imaging Radar Measurements of the Orbital Debris Environment: 2019,” NASA/TP-20210013669, April 2021.
- [2] Miller, R., Murray, J., Kennedy, T., “Goldstone Radar Measurements of the Orbital Debris Environment: 2018,” NASA/TP-20210015780, June 2021.
- [3] Stokely, C.L., Benbrook, J.R., Horstman, M., “On the Determination of Poisson Statistics for Haystack Radar Observations of Orbital Debris,” 58th International Astronautical Congress, Hyderabad, India, IAC-07-6.2.03, 2007.
- [4] Barton, D.K., Brillinger, D., El-Shaarawi, A.H., *et al*, “Final Report of the Haystack Orbital Debris Data Review Panel,” NASA/TM-1998-4809, February 1998.
- [5] Settecerri, T.J., Stansbery, E.G., Opiela, J.N., *et al*, “Haystack Radar Measurements of the Orbital Debris Environment; 1994 – 1996,” JSC-27842, May 1997.
- [6] Kennedy, T., Murray, J., “HUSIR Measurements of the OD Environment: 2014 – 2017,” *Orbital Debris Quarterly News*, Vol. 23, Issue 4, November 2019.
- [7] “History of On-Orbit Satellite Fragmentations, 15th Ed.,” NASA/TM-2018-220037, July 2018.
- [8] Vallado, D., *Fundamentals of Astrodynamics and Applications*, 4th Edition, Microcosm Press, pp. 177 – 194, 2013.